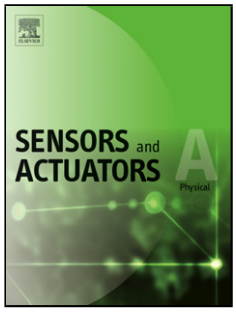

Title: Multi-frequency MEMS Electromagnetic Energy Harvesting

Authors: Dhiman Mallick, Peter Constantinou, Pranay Podder, Saibal Roy

PII: S0924-4247(16)31208-0
DOI: http://dx.doi.org/doi:10.1016/j.sna.2017.08.002
Reference: SNA 10256

To appear in: *Sensors and Actuators A*

Received date: 22-12-2016
Revised date: 14-6-2017
Accepted date: 1-8-2017

Please cite this article as: Dhiman Mallick, Peter Constantinou, Pranay Podder, Saibal Roy, Multi-frequency MEMS Electromagnetic Energy Harvesting, Sensors and Actuators: A Physicalhttp://dx.doi.org/10.1016/j.sna.2017.08.002

Multi-frequency MEMS Electromagnetic Energy Harvesting

Dhiman Mallick[1], Peter Constantinou[1], Pranay Podder[1], Saibal Roy[1,*]

[1]*Micro-nano-systems Center, Tyndall National Institute, Lee Maltings, Dyke Parade, Cork, Ireland*

[*]*Corresponding Author: saibal.roy@tyndall.ie*

Highlights:

- Multi-frequency MEMS electromagnetic energy harvesting using two novel topologies.
- Multi-frequency operation in the low frequency regime through design innovation.
- Overall improvement in the output power by using novel topologies compared to reported MEMS electromagnetic energy harvesters.
- Experimental results are qualitatively explained using the theoretical and finite element models.

Abstract: We report multi-frequency MEMS electromagnetic energy harvesters employing two different topologies. The first is a single mass system, where different fundamental modes are obtained within a close frequency range through spring design innovation and by using a large magnetic proof mass. The second is a dual mass system, which inherently has two major vibration modes corresponding to the movement of each of the masses. In comparison to the reported MEMS scale electromagnetic generators, substantial improvement in the output power is achieved in our design primarily by using the bulk NdFeB magnet as proof mass. This enhanced performance is validated by benchmarking against a normalized power density parameter. The spring structures are fabricated on Silicon-on-Insulator (SOI) substrate while voltage is induced in electroplated double layer copper coils. The 3D finite element analysis on the devices shows that different modes are activated in the low frequency region. The out-of-plane and torsional modes of the single mass systems are obtained at 188, 255.1 and 287.9 Hz, respectively whereas the first two modes of dual

mass device are at 241.4 Hz and 419.6 Hz respectively. At 0.5g, the single mass device produces 0.37, 0.43 and 0.32 μW respectively in mode I, II and III whereas the dual mass device generates 0.22 and 0.024 μW in mode I and II respectively against matched load. The experimental results are qualitatively explained using the simulation results and indicate a good potential in the development of multi-frequency energy harvesters for a number of practical applications.

I. Introduction:

Recently, Internet of Things (IoT) is regarded among the fastest growing technological platforms as it is predicted that there will be 25 billion of permanently connected things in few years' time. The potentials of such a wirelessly connected 'smart' world are huge as it would flourish the information and communications technology market, save time and resources, and provide opportunities for innovation and economic growth. The IoT is expected to make our environment safer and responsive by providing a wealth of information through new forms of automation. However, a critical issue that constricts this vision is powering of billions of wirelessly communicating devices. Energy harvesting presents a straightforward and long-term solution for powering those remote devices easily using clean energy. Among the different ambient energy sources, the research on harvesting electrical energy out of mechanical vibrations has surged in the last decade due to its abundance in our surrounding environment. The most commonly used transduction mechanisms for converting the available mechanical energy into the electrical energy are electromagnetic [1-3], piezoelectric [4-6] and electrostatic [7-9]. Regardless of the adopted transduction mechanisms, vibration energy harvesters (VEHs) are, in general, modelled using spring-mass-damper systems. Such systems are normally characterized by their resonant behaviour i.e., the peak output response is obtained at the resonance frequency but the response drops considerably with little shift of the ambient frequency from the resonance. In a number of practical applications, the operational condition is often unknown and the harvester with fixed resonant frequency is not suitable for such cases.

In order to address this problem, a number of strategies has been reported in literature to improve the efficiency of the energy harvesters under frequency varying environment, which can be categorized mainly under three sections - resonance frequency tuning [10-12], multi-frequency techniques [3, 13-14] and nonlinear energy harvesting [15-22]. Among these, multi-frequency techniques are most suitable for Micro-Electro-Mechanical System (MEMS) scale integration as most of the nonlinear energy harvesters require external components for their operation and

automatized resonance frequency techniques are very rare. The reported multi-frequency approaches can be classified in two major groups. The first group consists of an array of generators with different dimensions [3, 23] or different mass [24] to achieve separate resonance frequencies. Sari et al. [3], utilized an array of 35 parylene cantilevers with different lengths which are connected serially. An output power of 0.4 μW is obtained from the device with electromagnetic transduction mechanism working at the operating frequency range between 4.2 – 5 kHz. Ferrari et al. [24] reported similar array of cantilevers with piezoelectric bimorph structure which work at different frequencies below 300 Hz. The other group comprises of single structure with closely spaced vibration modes. Tadesse et al. [25] reported a multimodal generator with multiple (piezoelectric and electromagnetic) transduction mechanisms. The power output from the device is significantly increased as the electromagnetic transduction produces more power in the low frequency mode (20 Hz) whereas the piezoelectric method generates higher power in the second mode (300 Hz) due to the specific design of the device. Liu et al. [26] reported a MEMS electromagnetic multimodal generator where both in-plane and out-of-plane vibration modes are excited within a single structure where all of the modes are above 1 kHz. The same group reported another multi frequency MEMS electromagnetic structure [14] with similar mechanical functionality but different magnet coil arrangement. In a recent work [27], both the above mentioned approaches are combined so that an array of multi-frequency VEHs are reported where nine different frequency peaks are activated between 189 – 662 Hz within a single chip. The concept of coupled resonators with more than one proof mass was first proposed by Petropoulos et al. [28] in order to obtain flat response over a significant operating range by optimizing the different structural parameters. Wu et al. [29] reported a macro-scale, compact two degrees of freedom piezoelectric generator, where two vibration modes are developed due to two cantilever beams, one placed inside another, both operating at low frequencies. Tao et al. [30] recently reported MEMS EM two degrees of freedom VEH, which comprises of a primary subsystem for power generation and an accessory subsystem for frequency tuning where the device has two frequency peaks at 326 and 391 Hz, but the output power is lowered due to lower electromechanical coupling.

In this paper, two multi-frequency MEMS electromagnetic (EM) energy harvesting systems are studied. The first is a single mass system, where different fundamental modes are activated within a close range through design innovation and realization of the spring architectures on the thin Silicon-on-Insulator substrate. The second is a dual mass system, which inherently have two major vibration modes corresponding to the movement of each of the masses. First, a theoretical framework is developed for the single and dual mass energy harvesting devices along with description of design methodology and micro-fabrication processes. Then Finite Element Method

(FEM) simulations are provided to study the static and modal characteristics of the developed devices. Finally, the devices are characterized experimentally and the output responses are explained in terms of the FEM analysis provided.

II. Theoretical Model:

A single degree of freedom (SDOF), vibration based energy harvesting device is generally modelled as a second order spring mass damper system which was first proposed by Williams and Yates [31]. It consists of a mass mounted on a spring, which vibrates relative to a housing (fixed frame) when subjected to an external mechanical force. According to Newton's second law, the equation of motion of such system is given as

$$m\ddot{x}(t) + c\dot{x}(t) + kx(t) = -m\ddot{y}(t) \qquad (1)$$

Where x(t) is the relative displacement of the oscillator w.r.t. the fixed frame and m, c, k are respectively the mass of the oscillator, the total damping co-efficient which includes both mechanical/parasitic damping co-efficient (c_m) and electrical damping co-efficient (c_e) such that $c = c_m + c_e$, and spring stiffness of the system. For a sinusoidal input vibration of the form $y(t) = Ye^{i\omega t}$ (Where, Y = vibration amplitude and ω = frequency of vibration), the average output power can be derived from the above equation of motion as

$$P_{elec} = \frac{m\rho_e(\frac{\omega}{\omega_n})^3 Y^2 \omega^3}{[\{2\rho_T(\frac{\omega}{\omega_n})\}^2 + \{1-(\frac{\omega}{\omega_n})^2\}^2]} \qquad (2)$$

Where ρ_e and ρ_T are electrical and total damping ratios respectively and ω_n is the natural frequency. The above equation shows resonance behaviour i.e., the maximum output is obtained at the resonance frequency but the response drops as the external vibration frequency drifts from the resonance frequency.

Fig. 1 (a) on the other hand depicts the model of two degrees of freedom (TDOF) or dual mass system which requires two independent co-ordinates to describe the motion. The system consists of a primary and a secondary spring, at the end of each of which the primary and secondary masses are attached respectively. The coupled second order differential equation of motion for such system can be written in matrix form as

$$\begin{bmatrix} m_1 & 0 \\ 0 & m_2 \end{bmatrix} \begin{pmatrix} \ddot{x}_1 \\ \ddot{x}_2 \end{pmatrix} + \begin{bmatrix} c_1 + c_2 & -c_2 \\ -c_2 & c_2 \end{bmatrix} \begin{pmatrix} \dot{x}_1 \\ \dot{x}_2 \end{pmatrix} + \begin{bmatrix} k_1 + k_2 & -k_2 \\ -k_2 & k_2 \end{bmatrix} \begin{pmatrix} x_1 \\ x_2 \end{pmatrix} = \begin{pmatrix} f_1(t) \\ f_2(t) \end{pmatrix} \qquad (3)$$

Where $x_1(t)$ and $x_2(t)$ are the relative displacements of primary (m_1) and secondary (m_2) masses, c_1, c_2 are the damping co-efficients of primary and secondary oscillators and k_1 and k_2 are the effective primary and secondary spring stiffness values. The secondary damping c_2 also include the electromagnetic damping. For a sinusoidal input vibration of the aforementioned nature, the input forces on the right hand side of equation (3) can be written as $f_i(t) = -m_i\ddot{y}(t)$, i=1, 2.

Assuming a steady-state solution of equation (3) of the form $x_i(t) = X_i e^{i\omega t}$, it can be written,

$$\begin{pmatrix} X_1 \\ X_2 \end{pmatrix} = \frac{\begin{bmatrix} -\omega^2 m_2 + i\omega c_2 + k_2 & i\omega c_2 + k_2 \\ i\omega c_2 + k_2 & -\omega^2 m_1 + i\omega(c_1+c_2) + (k_1+k_2) \end{bmatrix}}{\begin{vmatrix} -\omega^2 m_1 + i\omega(c_1+c_2) + (k_1+k_2) & -i\omega c_2 - k_2 \\ -i\omega c_2 - k_2 & -\omega^2 m_2 + i\omega c_2 + k_2 \end{vmatrix}} \begin{pmatrix} m_1\omega^2 Y \\ m_2\omega^2 Y \end{pmatrix} \quad (4)$$

Solving the above matrix equation, the displacements of the primary and the secondary masses are

$$X_1(\omega) = \frac{(-\omega^2 m_2 + i\omega c_2 + k_2) m_1\omega^2 Y + (i\omega c_2 + k_2) m_2\omega^2 Y}{\begin{vmatrix} -\omega^2 m_1 + i\omega(c_1+c_2) + (k_1+k_2) & -i\omega c_2 - k_2 \\ -i\omega c_2 - k_2 & -\omega^2 m_2 + i\omega c_2 + k_2 \end{vmatrix}} \quad (5)$$

$$X_2(\omega) = \frac{(i\omega c_2 + k_2) m_1\omega^2 Y + (-\omega^2 m_1 + i\omega(c_1+c_2) + (k_1+k_2)) m_2\omega^2 Y}{\begin{vmatrix} -\omega^2 m_1 + i\omega(c_1+c_2) + (k_1+k_2) & -i\omega c_2 - k_2 \\ -i\omega c_2 - k_2 & -\omega^2 m_2 + i\omega c_2 + k_2 \end{vmatrix}} \quad (6)$$

The absolute values of the respective displacements are derived as

$$|X_1(\omega)| = \sqrt{\frac{((k_2 - \omega^2 m_2) m_1\omega^2 Y + k_2 m_2\omega^2 Y)^2 + (\omega^3 c_2 (m_1+m_2) Y)^2}{(k_1 k_2 + \omega^4 m_1 m_2 - \omega^2 (m_1 k_2 + m_2 k_1 + m_2 k_2))^2 + \omega^2 (m_1 c_2 + m_2 c_1 + m_2 c_2)^2}} \quad (7)$$

$$|X_2(\omega)| = \sqrt{\frac{((k_1 + k_2 - \omega^2 m_1) m_2\omega^2 Y + k_2 m_1\omega^2 Y)^2 + (\omega^3 c_2 (m_1+m_2) Y + \omega^3 c_1 m_2 Y)^2}{(k_1 k_2 + \omega^4 m_1 m_2 - \omega^2 (m_1 k_2 + m_2 k_1 + m_2 k_2))^2 + \omega^2 (m_1 c_2 + m_2 c_1 + m_2 c_2)^2}} \quad (8)$$

The generalized time response of the primary and secondary masses is given as

$$x_i(t) = |X_i(\omega)| e^{(i\omega t + \theta_i)}, i = 1, 2 \quad (9)$$

Where θ_i is the phase angle of the respective displacements which can be obtained from equations (5) and (6).

By setting the damping co-efficients and the external force to zero in equation (3), the resonance frequencies of the dual mass, two degrees of freedom system can be derived as

$$\omega_{n_{1,2}} = \sqrt{\frac{B \pm \sqrt{B^2 - 4 m_1 m_2 k_1 k_2}}{2 m_1 m_2}} \quad (10)$$

Where, $B = m_1k_2 + m_2(k_1 + k_2)$. If the forcing frequency is close to any of the resonance frequencies of the system, large displacement occurs leading to the large output power. In between the two resonances, there is one frequency where the displacement is however minimum. This phenomenon of anti-resonance has been utilized in a number of engineering problems to suppress the vibration of any structure. The most popular practical application of such 'tuned vibration absorber' is to solve London's Millennium bridge vibration problem [32]. However, we intend to take advantage of the two separate resonances of the TDOF system and increase the energy harvesting capabilities at different input frequencies. The total converted electrical power can be expressed as

$$p_{elec}(t) = c_e\omega|X_2(\omega)|^2 \qquad (11)$$

The effect of variation of different parameters on the performance of TDOF system is shown in Fig. 1 (b-d). Other parameters remaining same, the first and second frequency peaks shift towards the higher frequencies, and reduces in amplitude when the secondary mass (m_2) is significantly higher compared to the primary mass (m_1) as shown in Fig. 1 (b). On the other hand, comparatively low frequency and large amplitude peaks are obtained when m_1 is much higher than m_2 which is desirable in energy harvesting applications. It is observed from Fig. 1 (c) that the primary damping (c_1) changes the output response more significantly compared to the secondary damping (c_2) in terms of peak heights and quality factors. The peak amplitudes can be most effectively modulated through variation of spring constants. When secondary spring constant (k_2) is much larger than the primary spring constant (k_1), the first frequency peak is much larger compared to that of the second peak (Fig. 1 (d)). The difference between this amplitude becomes gradually small as k_1 is increased. When k_1 is much higher than k_2, the two peak amplitudes are approximately same. Therefore by optimizing different design parameters, the output response at two different frequencies can be significantly improved for multi-frequency energy harvesting purpose.

III. Design of the Multi-frequency MEMS Generators:

(a) Single Mass System: The designed system including the single mass spring structure is shown in Fig. 2. The central paddle (3×3 mm^2) is connected to the fixed frame using four L-shaped thin beams. The devices are fabricated on Silicon on Insulator (SOI) substrate which has a unique advantage i.e. the thickness of the spring arms can be defined by the device layer of SOI. The device layer thickness is set to 50 μm in this case. A small NdFeB block magnet (2.5×2.5×2 mm^3) is epoxy bonded onto the movable paddle which provides mass (9.83×10^{-5} Kg) to the vibrating

oscillator. Larger mass increases the generated power according to equation (2). In addition to increase in power, a large mass together with thin spring arms brings the fundamental vibration mode frequencies of the resonator down. Hence, the first few modes of the designed structure are obtained at a relatively low frequency (<300 Hz). The eigen-frequencies of the designed structure are analysed using finite element analysis software COMSOL Multi Physics and are shown in Fig. 3 (a-c), which are obtained at 180.2 Hz, 234.5 Hz and 245.3 Hz respectively. In the first mode, the device moves vertically, orthogonal to the device plane. However, in the second and third modes, it shows torsional movements in two opposite directions. The presence of multiple peaks in the close frequency range allows generating power from vibration sources with multiple peaks in their spectra. Detailed dimensions of the spring design are provided in Table 1.

(b) Dual Mass System: The dual mass system consists of two cantilevers which act as primary and secondary springs. But unlike the model shown in Fig. 1, where the secondary spring is extended away from the primary spring tip, here the secondary cantilever is curved inside the primary cantilever. The designed dual mass system along with compact spring structure is shown in the Fig. 4. It is observed from FEM analysis that if the secondary spring is extended outward from the edge of the primary spring, the gap between the fundamental frequencies of the two cantilevers becomes very large. Like the single mass device, this device is also fabricated on SOI substrate. The bulk silicon paddle at the end of the primary spring defines the primary mass whereas the silicon paddle along with an attached NdFeB magnet ($2\times2\times2$ mm^3) defines the secondary mass making it quite large compared to the primary mass. The eigen-frequency analysis of the dual mass harvester without and with the magnet is shown in Fig. 5 using COMSOL. The analysis shows that the first two fundamental frequencies of the spring structure without the magnet are at 945.8 Hz and 1218.1 Hz where the primary and secondary mass exhibits maximum displacements respectively. With the magnet attached, the first two fundamental modes appear at 227.2 Hz and 434.5 Hz respectively, where the secondary and primary masses undergo maximum displacements. An interesting observation here depicts that though the movements of the primary and secondary masses are in the out-of-plane direction, the tip of the magnet follows an arc of a circle with small angle, which can be approximated as an in-plane motion. Hence, the dual mass system offers three-dimensional energy harvesting capabilities, being out-of-plane in the first mode and in-plane in the second fundamental mode. Thus energy harvesting capabilities in different directions can be obtained from the same device. Different physical parameters for the designed device are tabulated in Table 2.

(c) Electromagnetic model: The relative motion between the static double-layer copper coil and the moving magnet is used to induce electrical voltage in the coil. According to the Faraday's law, the

electromotive force (EMF) induced in the coil is proportional to the negative rate of change of the magnetic flux experienced by the coil.

$$\varepsilon = -\frac{d\varphi}{dt} = -\frac{d}{dt}\sum_{i=1}^{N}(B.A_i) \qquad (12)$$

Where φ is the magnetic flux, N is the total number of turns in the coil, B is the magnetic flux density and A_i is the area included in the i-th loop. However, the magnetic flux is not same for both the in-plane and the out-of-plane movement of the magnet. For the single mass device, the magnet moves out-of-plane w.r.t the coil in the different vibration modes. However, the magnet motion is in-plane in the first mode and out-of-plane in the second mode for the dual mass system. The variation of the magnetic flux w.r.t the magnet displacement for both in-plane and out-of-plane motion is shown in Fig. 6. For in-plane motion, the magnetic flux becomes maximum when the magnet is in the center position. For out-of-plane motion, the magnetic flux becomes maximum when the magnet comes closest to the coil and reduces gradually as it moves away from the coil. Both the curves are fitted using third order polynomial functions as

$$\varphi = a_3x^3 + a_2x^2 + a_1x + a_0 \qquad (13)$$

Where $a_{3\text{-}0}$ are constants. The values of these constants for in-plane and out-of-plane movement of the magnet are given in Table 3. For a rectangular block magnet, the magnetic flux density (B) at a distance z along the line passing through the center of the magnet is given as [33]

$$B = \frac{B_r}{\pi}\left[\sin^{-1}\left[\frac{M_W M_L}{4[(\frac{M_W}{4}^2+z^2)(\frac{M_L}{4}^2+z^2)]^{1/2}}\right] - \sin^{-1}\left[\frac{M_W M_L}{4[(\frac{M_W}{4}^2+(z+M_T)^2)(\frac{M_L}{4}^2+(z+M_T)^2)]^{1/2}}\right]\right. \qquad (14)$$

Where B_r is the remnant magnetic flux density, M_L, M_W and M_T are length, width and thickness of the magnet respectively. In our designs, NdFeB N52 magnets with residual magnetic flux density (B_r) of 1.4 T are used. The inset of Fig. 6 shows the static magnetic flux line distribution along the cross-section of the magnet using Maxwell Ansoft 2D software.

IV. Microfabrication of the Energy Harvesting Devices:

Development of the designed MEMS based energy harvesters involves three major steps. First the multi-frequency MEMS spring structures are fabricated on Silicon-on-Insulator (SOI) substrate. Then the double layer, electroplated copper coils are fabricated on a separate silicon substrate. Finally the different components are assembled together to form the testing devices.

(a) Fabrication of Spring Structure on Silicon-on-Insulator (SOI): The micro-fabrication process flow of MEMS spring structures is shown in Fig. 7 along their cross-section. (i) This is a two mask fabrication process which starts with a 500 μm thick, double side polished Silicon-On-Insulator (SOI) wafer with a device layer of 50 μm, buried oxide layer (BOX) of 3 μm and a bulk handle layer of 450 μm respectively. (ii) 3 μm thick oxide layer is thermally grown using wet oxidation method in front and backside of the wafer. The front side oxide layer acts as the mask layer for the front device layer silicon etch whereas the back side oxide acts same for the back silicon etch. (iii) HiPR 6512 positive photoresist is spun on the front of the wafer, pattern was transferred using first mask and developed subsequently. This first mask is used to define the shape of the thin spring structure on the front side of the wafer. The front oxide layer is etched on the exposed sites using Plasma Enhanced Reactive Ion Etching (PERIE) to reach the device layer silicon. (iv) The resist is stripped off from the front and the same resist is spun on the back of the wafer and patterned using a second mask to etch the oxide layer for back silicon etching. (v) After etching of the back side oxide layer, the resist was stripped off. (vi) The device layer silicon in the front is etched using Deep Reactive Ion Etching (DRIE) up to the BOX layer to define the thin spring structure. 6 μm thick Al layer is sputtered in the front to provide mechanical support to the front silicon spring layer while the back silicon and oxide is etched sequentially. (vii) The handle layer silicon in the back is then etched using DRIE technique, followed by removal of the BOX layer. (viii) The wafer is diced and sputtered Al layer is wet etched using commercial etchant solution to release the mechanical structure.

The Scanning Electron Microscope (SEM) image of the single and double mass spring structures are shown in Fig. 8 (a) and 8 (c) respectively. The thin spring arms and bulk silicon masses are identified in the tilted images in Fig. 8 (b) and 8 (d).

(b) Fabrication of the double layer copper coil: The double layer electroplated copper coil is fabricated on a separate Silicon substrate and the corresponding process flow is also shown in Fig. 7, which is a three mask process. (i) The fabrication process starts by deposition of 1μm oxide layer on Si by wet oxidation followed by sputtering of Titanium/Copper (Ti/Cu) layer of 20/200 nm thickness which act as seed for electroplating. (ii) The substrate is then patterned using first mask after AZ9260 positive photoresist of 18.6 μm thickness is spin coated. The first layer of copper is electroplated up to 15 μm thickness using digital matrix plating line and the resist is stripped off. (iii) Then an optimized double spin coating process is used to develop 38 μm thick AZ9260 resist layer where the via layer is patterned using a second mask. The copper is again electroplated by 10 μm to fill the via. (iv) After the resist is stripped and seed layers are etched, SU-8 insulation layer is spun to a thickness of 28 μm to isolate the bottom copper tracks from the top layer. Similar seed

layers (Ti/Cu) as the bottom is sputtered again on SU-8. (v) The corresponding layer is patterned using a third mask using AZ9260 resist (19 μm thick) again and then top layer copper is electroplated up to a height of 12.5μm. Similar to the bottom layer, the resist is stripped off and seed layers are etched using HF acid. Finally another layer of SU-8 (28 μm thick) is spun to provide passivation to the structure.

The electroplated copper tracks after first layer of coil deposition is depicted in Fig. 9 (a) using SEM imaging. The cross-sectional image of the complete two layer coil is shown in Fig. 9 (b), which clearly shows the two conductive copper layers of the coil connected at the middle.

(c) Device Packaging: The magnets are epoxy bonded on the silicon paddle under the optical microscope in a relatively precise manner. Using finite element analysis, it has been observed that a slight mismatch in the alignment of center of magnet with that of the coil does not affect the output significantly [48]. The image of the packaged single mass and double mass devices are shown in Fig. 10 (a) and 10 (b) respectively where each of the packaged devices has a volume of 0.14 cm^3.

III. EXPERIMENTAL RESULTS AND DISCUSSIONS:

(a) Experimental Procedure:

The fabricated devices are experimentally characterized using a test set up which comprises a Brüel & Kjær LDS V455 computer controlled Permanent Magnet Shaker, an LDS Comet USB vibration control system, an LDS PA 1000L power amplifier and an oscilloscope (Picoscope 3000 series). The sweeping sinusoidal signal is produced by the vibration controller via the power amplifier to get a constant input acceleration level which is monitored by a miniature piezoelectric CCLD accelerometer (LDS 4394). Since the expected output signals from the devices are very low (as in the case for most MEMS EM VEH devices), the devices and the bread board circuit consisting of the electrical loads are encapsulated within a ground-connected aluminium box to minimize the effect of external electromagnetic noise on the device output. The grounded aluminium enclosure including the device and load circuitry is placed on a vibrating stage attached to the shaker which generates sinusoidal excitation in the vertical direction. The devices are tested under different input acceleration levels (0.05g – 1g, 1g = 10 m/s^2) while the input frequency is varied in each case.

(b) Characterization of the Single Mass Device (SMD):

The open circuit voltage time trace for the generator is shown in Fig. 11 (a) where the input frequency is swept from 100 to 300 Hz at 0.5g at a rate of 1.67 Hz/sec. The three peaks denote the three fundamental modes of the MEMS spring structure. The corresponding RMS open circuit

voltage frequency response (Fig. 11 (b)) is obtained using the Fast Fourier Transform (FFT) technique of the time domain data. Three voltage peaks of 14.8, 17.05 and 16.8 mV are obtained at the resonance frequencies of 188, 255.1 and 287.9 Hz, respectively. Based on the modal analysis results shown in Fig. 3, these three frequencies actually correspond to the out-of-plane motion (mode I) at 180.2 Hz, torsion motion (mode II) at 234.5 Hz and torsion motion in another direction (mode III) at 245.3 Hz, respectively. The obtained modal frequencies match reasonably well with the experimental results but the observed deviation could be due to the slight geometrical variation of the spring structure during the DRIE etch process.

The variation of the RMS open circuit voltage with the input acceleration is shown in the Fig. 12 where the output voltage increases with the input excitation level as expected being only 4.2, 2.6 and 2.8 mV at 0.05g for the three different resonance modes which rises up to 17, 29.7 and 21.3 mV at 1g. It is to be noted here the output response from the three modes are comparable in amplitude. Although the device is designed for large out-of-plane motion, the attached large magnet mass could possibly aid the torsional movements in mode 2 and 3 which helps in achieving large output from those two modes as well. The open circuit quality factors of the resonant energy harvesting system are 38.69, 80.91 and 59.92 in the three different modes respectively which are calculated using the formula $Q_{OC} = \frac{f_r}{f_2 - f_1}$ where f_r is the resonance frequency and f_1 and f_2 are lower and higher cut-off frequencies.

Next, load resistance is connected to the generator to dissipate electrical power. The variation of the load power of the three modes with the load resistance is shown in Fig. 13 (a). The matched load is found to be 190 Ω which is quite close to the coil resistance (R_C = 187 Ω) value. As described earlier, if the magnetic flux linkage is small so that the electromagnetic damping co-efficient is much lower than the mechanical damping, then the maximum load power is obtained when the resistive load is equal to the coil resistance. The maximum power of 0.37, 0.43 and 0.32 μW are obtained at the matched load for input acceleration of 0.5g which rises to 0.6, 1.5 and 0.9 μW respectively at 1g as shown in Fig. 13 (b).

(c) Characterization of the Dual Mass Device (DMD):

The time history of the DMD under no-load condition is depicted in Fig. 14 (a) as the input vibration frequency is varied from 100 to 500 Hz at a fixed acceleration of 0.5g at the same rate as that mentioned for the SMD. It is observed from the time trace that the large amplitude voltage peak is generated at the lower frequency which is due to the large amplitude motion of the magnet in the low frequency mode, creating higher electromagnetic flux linkage. On the contrary, the range of

motion of the magnet is much smaller in the high frequency mode as observed from the modal analysis in Fig. 5(d), and produces much lower voltage. From the FFT plot in Fig. 14 (b), the two peaks are generated at 241.4 Hz and 419.6 Hz respectively. The experimentally obtained frequencies are close to simulated modal frequencies of 227.2 Hz and 434.5 Hz. Similar to the SMD case, here also the reason of discrepancy could be due to the mismatch between the designed and the fabricated geometric parameters. The calculated open circuit quality factors (Qoc) of the two modes are 46.28 and 39.33 respectively.

The load power variation of the two natural modes of the device for varying load resistance (R_L) is shown in Fig. 15(a) at an acceleration of 0.5g. The matched load in this case is also equal to the internal load of the coil (R_C=191 Ω). In the first mode, the maximum electrical power that is transferred to the load is 0.22 μW. That value reduces to 0.024 μW in the second vibration mode due to the aforementioned reason. The maximum load power rises to 1.13 μW and 0.066 μW respectively at 1g acceleration respectively as shown in Fig. 15 (b).

Table 4 summarizes the results and provides a comparative study between the output performances of the SMD and DMD respectively.

(d) Benchmarking:

Comparing different VEHs is not straightforward as the amount of data presented in published works varies considerably in terms of their operating conditions such as input acceleration and frequency. Hence, direct comparison of the output electrical parameters such as voltage, current or power is not justified. Beeby et al [34] derived a figure-of-merit for resonant VEH devices called, Normalized Power Density (NPD), which is simply the output power (P) of the device normalized w.r.t. input acceleration level (A) and volume (V) of the device. Frequency is not considered in the figure-of-merit as resonant generators are fixed in frequency whereas acceleration levels applied during testing can be varied. NPD can be defined as

$$NPD = \frac{P}{A^2 V} \qquad (15)$$

It is to be noted that acceleration (A) is taken in equation (15) in square form as the power varies with square of acceleration as mentioned in equation (2). In Fig. 16, the NPD of different MEMS scale EM energy harvesters are compared w.r.t their operating frequency (Fig. 16(a)) and device volume (Fig. 16(b)). It is to be noted here, we have compared different MEMS scale VEH devices regardless of their operating principles, including resonant, multi-frequency and nonlinear energy harvesters. For wideband nonlinear devices, the peak power generated at the down jump frequency

is considered which is not fully justified but makes the comparison easy. In terms of the level of integration, the fully integrated MEMS EM harvesters [35-41] have lowest NPD due to the low efficiency of the integrated magnets. Integration of thick permanent magnet while retaining their performance comparable to that of bulk magnets is a challenging task which has been undertaken in a number of reported works and is a major field of research [49-51]. Thus in most of the reported literatures [1-3, 14, 19, 26-27, 42], bulk NdFeB magnets are used whereas the spring structure and pick-up coils are integrated using CMOS compatible MEMS techniques. Coils are mostly integrated on the vibrating elements while a single or an array of static magnet is used to create the varying magnetic field. The output power is found to be low in such cases due to poor magnetic flux linkage and smaller proof mass. In some reported literatures [1, 14, 19, 26-27], sputtered metallic coil is used to induce electrical voltage. Generally the thickness of the sputtered layers is quite low which affect the final output. Silicon is the most commonly used material in MEMS devices due to their suitability with CMOS compatible fabrication processes and its mechanical robustness. But due to its large elastic modulus (Y=170 GPa), the operational frequency increases significantly with dimensional miniaturization. Hence, many researchers have exploited other polymeric materials like PDMS [39, 44] and parylene [3, 43] for development of the spring structure in order to reduce the resonance frequency within the same footprint. The low Young's modulus not only brings the resonance frequency to a lower value but also increases the displacement amplitude as the spring constant is reduces. However, reliability of these materials for long term applications is a concern which is yet to be verified in reported literatures.

In this reported work, a magnet proof mass architecture is used where NdFeB bulk magnet is bonded on the silicon paddle to increase the mass as well as the output power. The high performance obtained from the MEMS energy harvesters is also due to the development of integrated, double layer, and thick copper micro-coil, which enhances the electromagnetic coupling with the moving magnet. This factors lead to the NPDs of 0.0429, 0.1071 and 0.0643 kg.s/m^3 respectively in the first three vibration modes of SMD and 0.0807 and 0.0047 kg.s/m^3 respectively in the first two modes of the DMD, which are among the higher values for MEMS scale EM VEH devices. The performances can further be improved through even more optimization of the different design parameters as described in the theoretical model section. With further improvements, the reported devices can be employed in a number of practical applications where the input vibration consists of multiple frequency peaks below 1 kHz [47, 52]. Power requirement in such applications are further reduced by optimizing the active and sleep mode duty cycles of operation of the sensors. Thus, the proposed methodology can be applied with required modifications for efficient and perpetual energy supply in numerous IoT based emerging applications.

VI. Conclusions:

This paper investigates the potential of multi-frequency MEMS EM VEH devices for a number of practical applications employing two different topologies. The first system is a single mass topology, where different fundamental modes are obtained within a close range through spring design innovations. The second system is a dual mass topology, which inherently have two major vibration modes corresponding to the movement of each of the masses. The output power is improved in our designs in general by using the bulk magnet as proof mass compared to the reported MEMS scale EM generators. The 3D finite element analysis on the devices shows that different modes are activated in the low frequency region. The out-of-plane and torsional modes of the single mass systems are obtained at 188, 255.1 and 287.9 Hz, respectively whereas the first two modes of dual mass device are at 241.4 Hz and 419.6 Hz respectively. The spring structures are fabricated using Silicon-on-Insulator (SOI) substrate while moving magnets attached to the spring induce voltage in the electroplated double layer copper coils fabricated on silicon substrate. At 0.5g, the single mass device produces 0.37, 0.43 and 0.32 μW respectively in mode I, II and III whereas the dual mass device generates 0.22 and 0.024 μW in mode I and II respectively against matched load. The experimental results are qualitatively explained using the simulation results. Finally, the high performances of the reported devices are benchmarked against the existing MEMS scale EM VEH devices using 'normalized power density' figure-of-merit.

VII. Acknowledgement:

This work is financially supported by Science Foundation Ireland (SFI) Principal Investigator (PI) project on 'Vibration Energy Harvesting' -grant no SFI-11/PI/1201. The authors would also like to thank Central Fabrication Facilities at Tyndall National Institute for the fabrication part.

References:

1. H. Liu, K. H. Koh and C. Lee, "Ultra-wide frequency broadening mechanism for micro-scale electromagnetic energy harvester", Appl. Phys. Lett., **104**, 053901 (2014).
2. S. Kulkarni, E. Koukharenko, R. Torah, J. Tudor, S. Beeby, T. O'Donnell, S. Roy,' Design, fabrication and test of integrated micro-scale vibration-based electromagnetic generator', Sens. Actuators A, 145–146:336–342 (2008).
3. I. Sari, T. Balkan and H. Kulah, 'An electromagnetic micro power generator for wideband environmental vibrations', Sens. Actuators A, 145-146:405-13 (2008).
4. A. Erturk and D. J. Inman, "An experimentally validated bimorph cantilever model for piezoelectric energy harvesting from base excitations", Smart Mater. Struct. 18 025009 (2009).
5. R. Elfrink, T. M. Kamel, M. Goedbloed, S. Matova, D. Hohlfeld, Y. V. Andel and R. V. Schaijk, "Vibration energy harvesting with aluminum nitride-based piezoelectric devices", J. Micromech. Microeng. 19 094005 (2009).
6. S A. Hajati and S-G Kim, "Ultra-wide bandwidth piezoelectric energy harvesting", Appl. Phys. Lett. 99, 083105 (2011).
7. P.D. Mitcheson, P. Miao, B.H. Stark, E.M. Yeatman, A.S. Holmes, and T.C. Green, "MEMS electrostatic micropower generator for low frequency operation", Sens. Actuators A, 115, Issues 2–3, Pages 523–529 (2004).
8. S. D. Nguyen, E. Halvorsen, "Nonlinear Springs for Bandwidth-Tolerant Vibration Energy Harvesting", J. Microelectromech. Syst., 20, 1225 - 1227 (2011).
9. P. Basset, D. Galayko, F. Cottone, R. Guillemet, E. Blokhina, F. Marty, T. Bourouina, "Electrostatic vibration energy harvester with combined effect of electrical nonlinearities and mechanical impact", J. Micromech. Microeng., 24, 035001 (2014).
10. S. E. Leland and P. K. Wright, 'Resonance Tuning of Piezoelectric Vibration Energy Scavenging Generators Using Compressive Axial Preload', Smart Mater. Struct., 15:1413-20 (2006).
11. V. R. Challa, M. G. Prasad, Y. Shi and F. T. Fisher, "A vibration energy harvesting device with bidirectional resonance frequency tenability", Smart Mater. Struct., 17:015035 (2008).
12. D. Mallick, S. Roy, "Bidirectional electrical tuning of FR4 based electromagnetic energy harvesters", Sens. Actuators A, 226, 154-162 (2015).

13. B. Yang, C. Lee, W. Xiang, J. Xie, J. H. He, R. K. Kotlanka, S. P. Low and H. Feng, "Electromagnetic energy harvesting from vibrations of multiple frequencies", J. Micromech. Microeng., 19:035001 (2009).

14. H. Liu, Y. Qian, C. Lee, "A multi-frequency vibration-based MEMS electromagnetic energy harvesting device", Sens. Actuators A 204: 37-43 (2013).

15. F. Cottone, H. Vocca and L. Gammaitoni, "Nonlinear energy harvesting", Phys. Rev. Lett., 102, 080601 (2009).

16. S. C. Stanton, C. C. McGehee and B. P. Mann, "Nonlinear dynamics for broadband energy harvesting: Investigation of a bistable piezoelectric inertial generator", Physica D, 239, 640-53 (2010).

17. A. Erturk, J. Hoffmann and D. J. Inman, "A piezomagnetoelastic structure for broadband vibration energy harvesting", Appl. Phys. Lett., 94, 254102 (2009).

18. B. P. Mann and N. D. Sims, "Energy harvesting from the nonlinear oscillations of magnetic levitation", J. Sound Vib., 319, 515-30 (2009).

19. H. Liu, Y. Qian, N. Wang and C. Lee, "An in-plane approximated nonlinear MEMS electromagnetic energy harvester", J. Microelectromech. Syst., 23, 740-749 (2014).

20. S. C. Stanton, C. C. McGehee, and B. P. Mann, "Reversible hysteresis for broadband magnetopiezoelastic energy harvesting", Appl. Phys. Lett., 95, 174103 (2009).

21. D. Mallick, A. Amann and S. Roy, "A nonlinear stretching based electromagnetic energy harvester on FR4 for wideband operation", Smart Mater. Struct., 24:015013 (2015).

22. Y. Lu, F. Cottone, S. Boisseau, F. Marty, D. Galayko and P. Basset, "A nonlinear MEMS electrostatic kinetic energy harvester for human-powered biomedical devices", Appl. Phys. Lett. 107, 253902 (2015).

23. J-Q. Liu, H-B. Fang, Z-Y. Xu, X-H. Mao, X-C. Shen, D. Chen, H. Liao, B-C. Cai, 'A MEMS-based piezoelectric power generator array for vibration energy harvesting', Microelect. Journ., 39:802–806 (2008).

24. M. Ferrari, V. Ferrari, M. Guizzetti, D. Marioli, A Taroni, 'Piezoelectric Multifrequency Energy Converter for Power Harvesting in Autonomous Microsystems', Sens. Actuators, A: Phys, 142:329-335 (2008).

25. Y. Tadesse, S. Zhang, S. Priya, 'Multimodal Energy Harvesting System: Piezoelectric and Electromagnetic', J. Intell. Mater. Syst. Struct., 20:625-632 (2009).

26. H. Liu, B. W. Soon, N. Wang, C. J. Tay, C. Quan, C. Lee, 'Feasibility study of a 3D vibration-driven electromagnetic MEMS energy harvester with multiple vibration modes', J. Micromech. Microeng. 22:125020 (2012).

27. H. Liu, T. Chen, L. Sun, C. Lee, 'An Electromagnetic MEMS Energy Harvester Array with Multiple Vibration Modes', Micromachines, 6:984-992 (2015).

28. T. Petropoulos, E. M. Yeatman, P. D. Mitcheson, 'MEMS coupled resonators for power generation and sensing', Proc. Micromech. Europe, Leuven, Belgium (2004).

29. H. Wu, L. Tang, Y. Yang, C. K. Soh, 'A novel two-degrees-of-freedom piezoelectric energy harvester', J. Intell. Mat. Syst. Struc., 1045389X12457254 (2012).

30. K. Tao, J. Wu, L. Tang, X. Xia, S. W. Lye, J. Miao, X. Hu, 'A novel two-degree-of-freedom MEMS electromagnetic vibration energy harvester', J. Micromech. Microeng., 26:035020 (2016).

31. C. B. Williams, M. A. Shearwood Harradine, P. H. Mellor, T. S. Birch, R. B. Yates, Development of an electromagnetic micro-generator, IEE Proc. Circuits Devices Syst.148:337–42 (2001).

32. P. Dallard, T. Fitzpatrick, A. Flint, A. Low, R. R. Smith, M. Willford, M. Roche, 'london millennium bridge: pedestrian-induced lateral vibration', J. Bridge Engg., 6(6):412-417 (2001).

33. J. Svoboda, Magnetic Techniques for the Treatment of Materials (Dordrecht: Kluwer) pp 260–3 (2004).

34. S. P. Beeby, R. N. Torah, M. J. Tudor, P. Glynne-Jones, T. O'Donnell, C. R. Saha and S. Roy, A micro electromagnetic generator for vibration energy harvesting, J. Micromech. Microeng. 17, 1257–1265 (2007).

35. Y. Jiang, S. Masaoka, T. Fujita, M. Uehara, T. Toyonaga, K. Fujii, K. Higuchi, K. Maenaka, 'Fabrication of a vibration-driven electromagnetic energy harvester with integrated NdFeB/Ta multilayered micro-magnets', J. Micromech. Microeng., 21: 095014 (2011).

36. Y. Tanaka, T. Fujita, T. Kotoge, K. Yamaguchi, K. Sonoda, K. Kanda, K. Maenaka, 'Electromagnetic Energy Harvester by Using NdFeB Sputtered on High Aspect Ratio Si Structure', J. Phys.: Conf. Ser. 476:012095 (2013).

37. M. Han, Z. Li, X. Sun, H. Zhang, 'Analysis of an in-plane electromagnetic energy harvester with integrated magnet array', Sens. Act. A: Phys., 219:38–46 (2014).

38. M. Han, Q. Yuan, X. Sun, H. Zhang, 'Design and Fabrication of Integrated Magnetic MEMS Energy Harvester for Low Frequency Applications', IEEE J. Microelectromech. Syst., 23(1):204-212 (2014).

39. N. Wang, D. P. Arnold, 'Fully batch-fabricated MEMS magnetic vibration energy harvesters', Proc. PowerMEMS 2009, Washington DC, USA, pp 348-51 (2009).

40. Q. Zhang, E. S. Kim, 'Micromachined Energy-Harvester Stack with Enhanced Electromagnetic Induction Through Vertical Integration of Magnets', IEEE J. Microelectromech. Syst., 24(2):384-394 (2015).

41. S. Miki, T.Fujita, T. Kotoge, Y.G. Jiang , M. Uehara, K. Kanda, K. Higuchi, K. Maenaka, 'Electromagnetic energy harvester by using buried NdFeB', IEEE 25th International Conference on Micro Electro Mechanical Systems (MEMS), Paris, pp. 1221-1224 (2012).

42. Q. Zhang, E. S. Kim, 'Microfabricated Electromagnetic Energy Harvesters With Magnet and Coil Arrays Suspended by Silicon Springs, IEEE Sensor Journ., 16(3):634-641 (2016).

43. Ö. Zorlu, H. Külah, 'A MEMS-based energy harvester for generating energy from non-resonant environmental vibrations', Sens. Actuators A, 202:124–134 (2013).

44. F. Khan, F. Sassani, B. Stoeber, 'Nonlinear behaviour of membrane type electromagnetic energy harvester under harmonic and random vibrations', Microsyst. Technol., 20:1323–1335(2014).

45. P. Wang, H. Liu, X. Dai, Z. Yang, Z. Wang, X. Zhao, 'Design, simulation, fabrication and characterization of a micro electromagnetic vibration energy harvester with sandwiched structure and air channel', Microelectron. Journ., 43:154–159 (2012).

46. F. Khan, F. Sassani, B. Stoeber, 'Copper foil-type vibration-based electromagnetic energy harvester', J. Micromech. Microeng. 20:125006 (2010).

47. S. P. Beeby, L. Wang, D. Zhu, A. S. Weddell, G. V. Merrett, B. Stark, G. Szarka, B. M. Al-Hashimi, 'A comparison of power output from linear and nonlinear kinetic energy harvesters using real vibration data', Smart Mater. Struct., 22:075022 (2013).

48. D. Mallick, A. Amann, S. Roy, 'High Figure of Merit Nonlinear Microelectromagnetic Energy Harvesters for Wideband Applications', J. Microelectromech. Syst., 26(1): 273-282 (2017).

49. D. P. Arnold, N. Wang, 'Permanent magnets for MEMS' J. Microelectromech. Syst. 18(6):1255-1266 (2009).

50. D. Niarchos, 'Magnetic MEMS: key issues and some applications', Sens. Act. A: Phys.: 109(1):166-173 (2003).

51. O. Cugat, J. Delamare, G. Reyne, 'Magnetic micro-actuators and systems (MAGMAS)', IEEE Trans. Magn., 39(6):3607-3612 (2003).

52. R. Rantz, S. Roundy, 'Characterization of Real-world Vibration Sources and Application to Nonlinear Vibration Energy Harvesters', Energy Harv. Syst., 4(2):67-76 (2017).

Dhiman Mallick was born in Kolkata, India in 1986. He received the B.Tech. and M.Tech. degrees in Radio Physics and Electronics Engineering from University of Calcutta, Kolkata, India, in 2010 and 2012, respectively. He joined Tyndall National Institute, University College Cork, Ireland in October, 2012 as doctoral research student and currently holding that position. He has been awarded the UCC Strategic Research Fund PhD studentship award in 2014 by University College Cork. His research interests include Vibrational Energy Harvesting, MEMS based Energy Harvesters, Magnetic thin films and nanostructures and MEMS based actuators.

Peter Constantinou was born in Limassol, Cyprus, in 1982. He received the M.Eng. degree in avionic systems and the Ph.D. degree in electrical and electronic engineering from the University of Bristol, Bristol, U.K. in 2004 and 2009, respectively. He is currently a Sensor Technologist at TT Electronics plc, Cambridge, U.K. Research Associate in the. He has held various research positions at Tyndall National Institute, Cork, Ireland; Nanoscience Center at University of Cambridge, Cambridge, UK; Faculty of Computing, Engineering and Technology at Staffordshire University, Stafford, U.K.; and in the Department of Electrical and Electronic Engineering at the University Bristol. His research interests include sensor development, energy harvesting systems, wireless sensor nodes, and linear actuators.

Pranay Podder received the B.Tech. and M.Tech. degrees in radio physics and electronics engineering from the University of Calcutta, Kolkata, India, in 2010 and 2012, respectively. He joined Tyndall National Institute, University College Cork, Cork, Ireland, in January, 2013, where he is currently working toward the Ph.D. degree. His research interests include vibrational energy harvesting, MEMS-based energy harvesters, nonlinear mechanics, hard and soft magnetic materials, and microfluidic MEMS for biomedical applications.

Saibal Roy is Science Foundation Ireland Principal Investigator (SFI PI) and Head of Micropower Systems & Nanomagnetics at Tyndall National Institute, Ireland. He obtained his M.Sc. degree in Physics from the IIT and Ph.D. from IACS in India. His professional experiences include 18 years academic and 3 years industrial experience as head of research groups. In 2013, Dr. Roy was hosted by Electrical Engineering Department, Stanford University in a sabbatical visit. In 2015, Dr. Roy has been awarded the prestigious visiting Chair Professorship in engineering (Prof A S Paintal Chair) by INSA (Indian National Science Academy), Govt. of India. Dr. Roy's present research interests include investigating how engineered nanostructures could be employed for the benefits of micron scale devices. To date, he has 3 patents, written 7 book chapters and over 160 papers in Journals and peer reviewed conference proceedings with h-index of 27.

Figures:

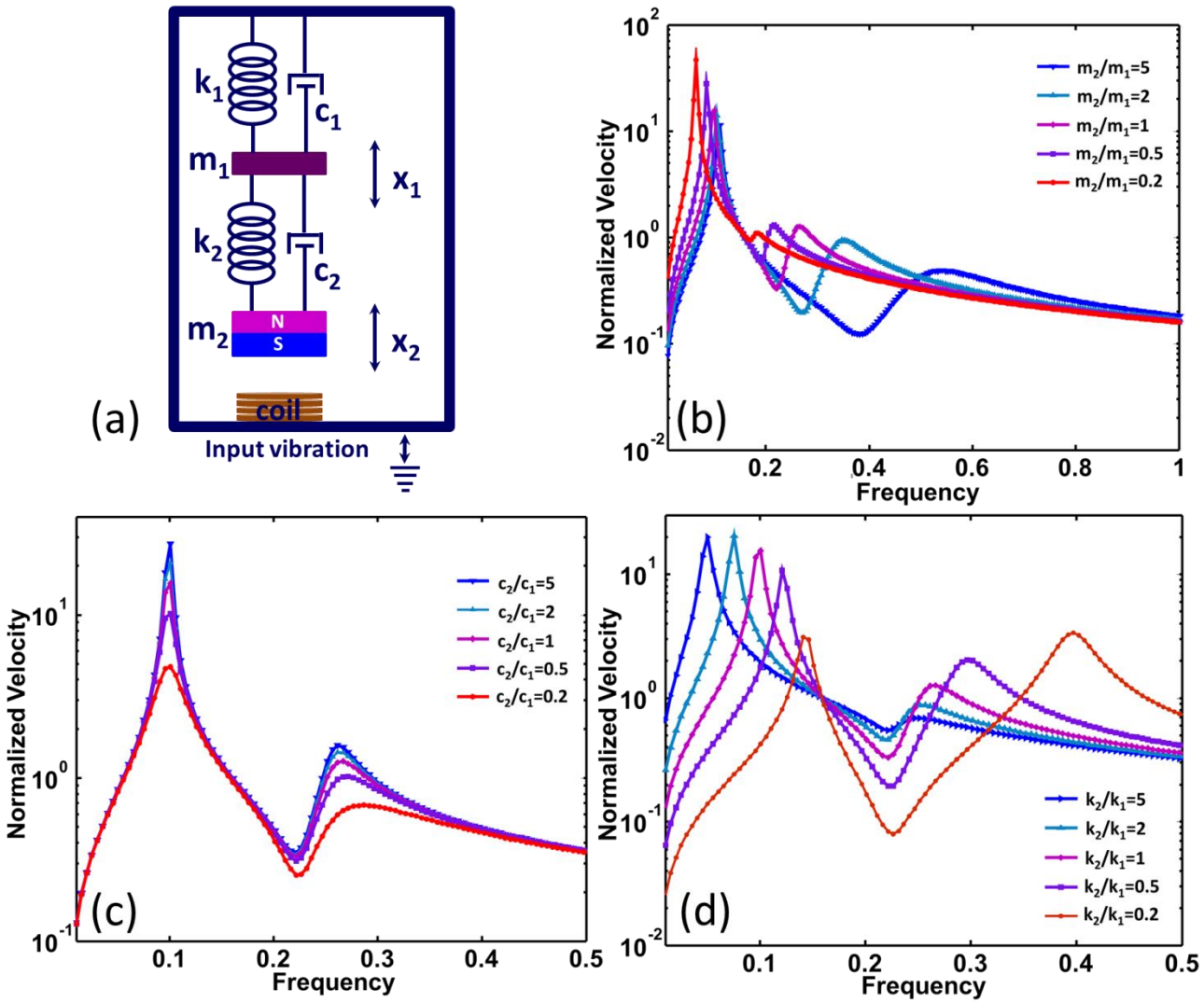

Fig. 1: (a) Model of a Two Degrees-of-freedom (TDOF) system. Parametric study of the TDOF system: (b) m_2/m_1, (c) c_2/c_1 and (d) k_2/k_1 are changed while other parameters are kept constant.

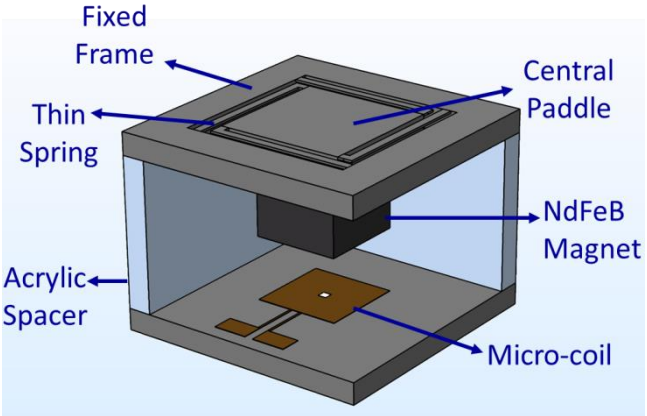

Fig. 2: Schematic depiction of the Single Mass Device (SMD). For clarity, the spacer is not shown on the front sides.

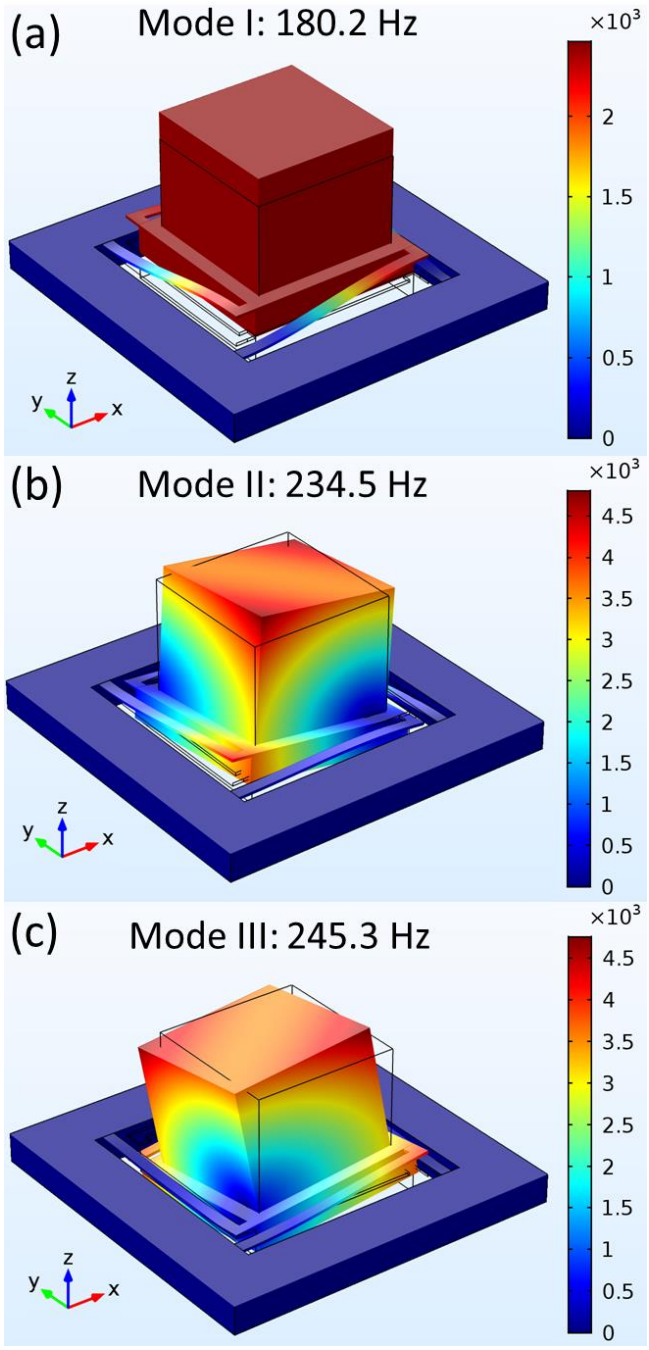

Fig. 3: First three fundamental modes of SMD from COMSOL - (a) Mode I: Vertically up and down movement, (b) Mode II: Torsional motion, (c) Mode III: Another torsional movement.

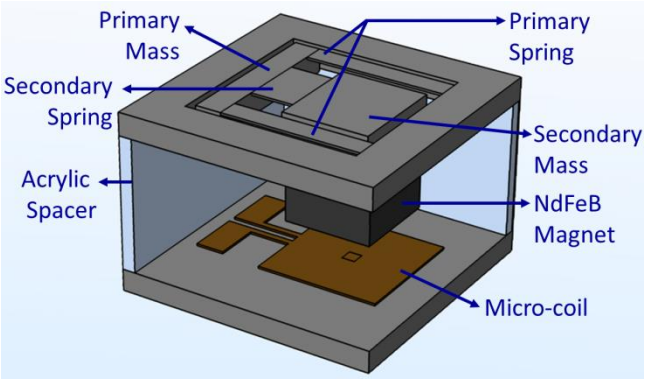

Fig. 4: Schematic depiction of the Dual Mass Device (DMD). For clarity, the spacer is not shown on the front sides.

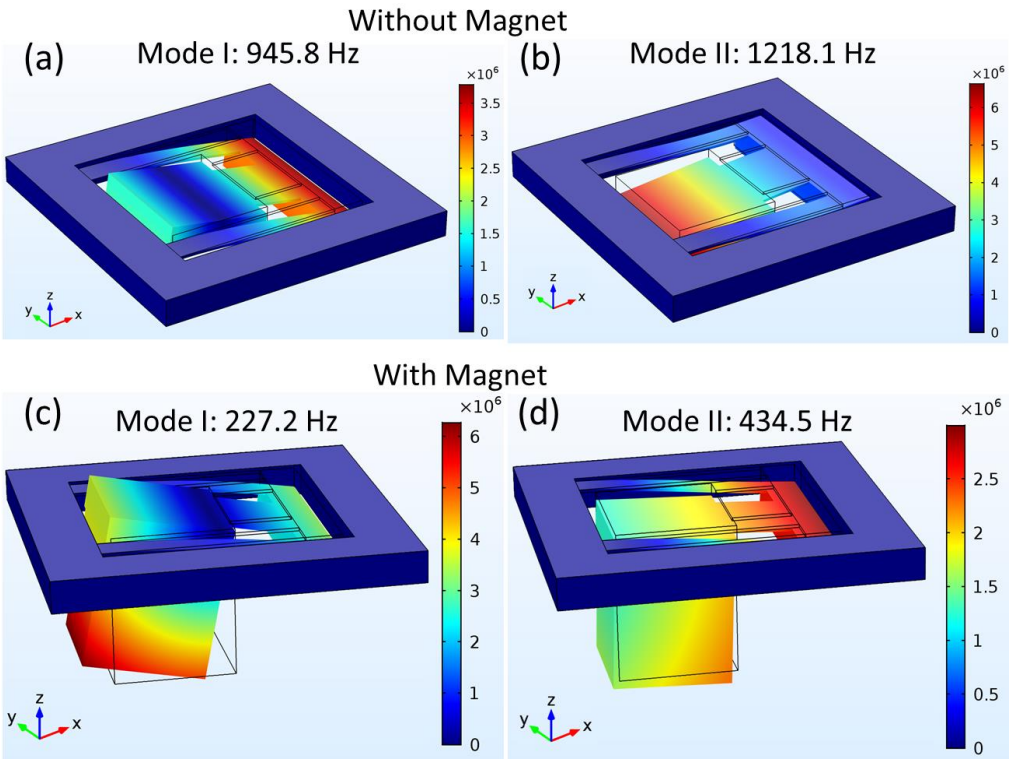

Fig. 5: First two fundamental modes of DMD without [(a) and (b)] and with [(c) and (d)] the magnet from COMSOL – The primary mass undergoes the maximum displacement in mode I without the magnet whereas secondary mass undergoes maximum displacement in mode II. This reverses in presence of the magnet mass.

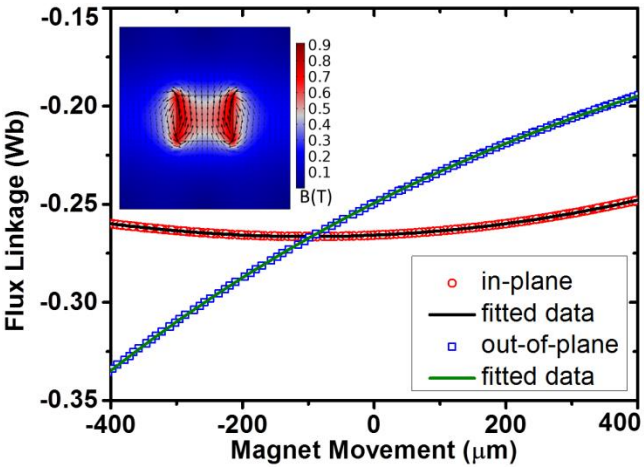

Fig. 6: Flux linkage variation for in-plane and out-of-plane motion of the magnet. The inset shows the static magnetic flux distribution of the magnet.

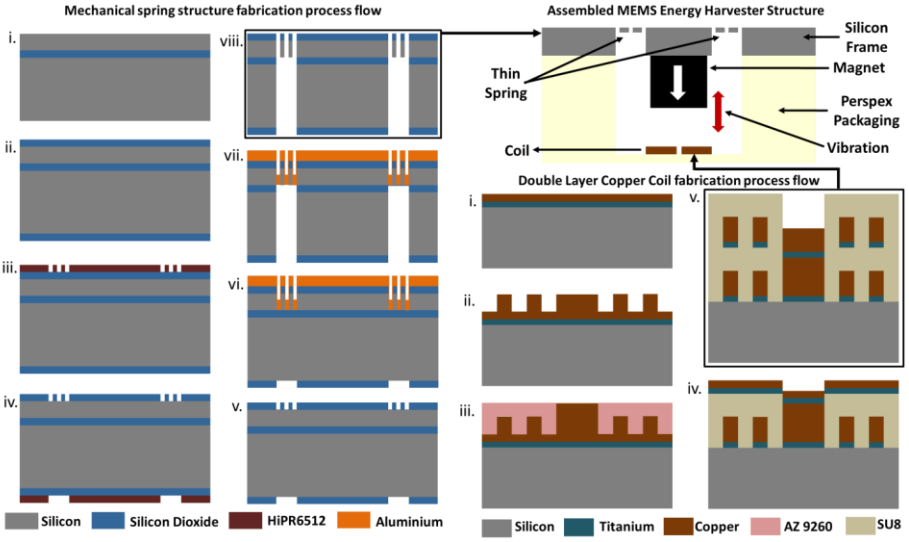

Fig. 7: Three level Fabrication process flow for the MEMS EM Harvesters: Fabrication of the spring structures on SOI, Fabrication of the double layer copper coil, Assembly and packaging of the individual components.

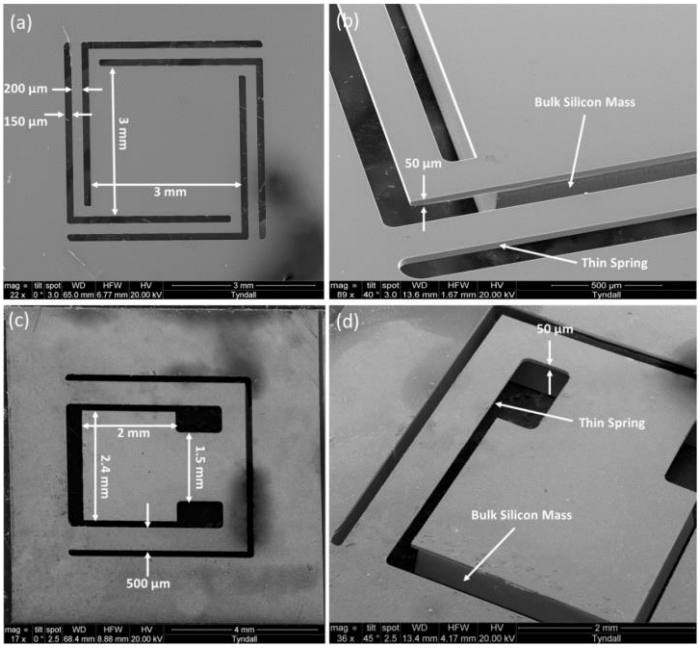

Fig. 8: SEM images of the (a) Single mass spring structure (b) Corresponding tilted image showing bulk silicon mass and thin spring.(c) Double mass spring structure (d) Corresponding tilted image.

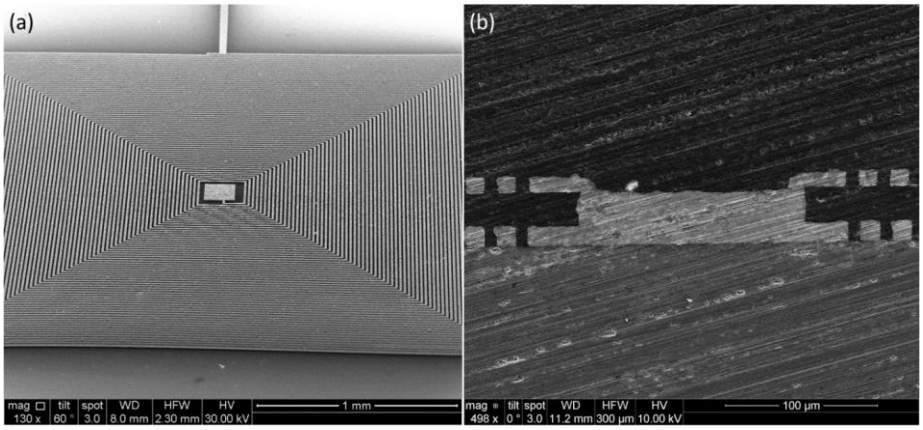

Fig. 9: SEM image of the micro-coil after bottom layer development which shows one electrical connection and central pad for via development. (b) SEM image of the cross-section of the coil indicating two layers of copper and a via layer.

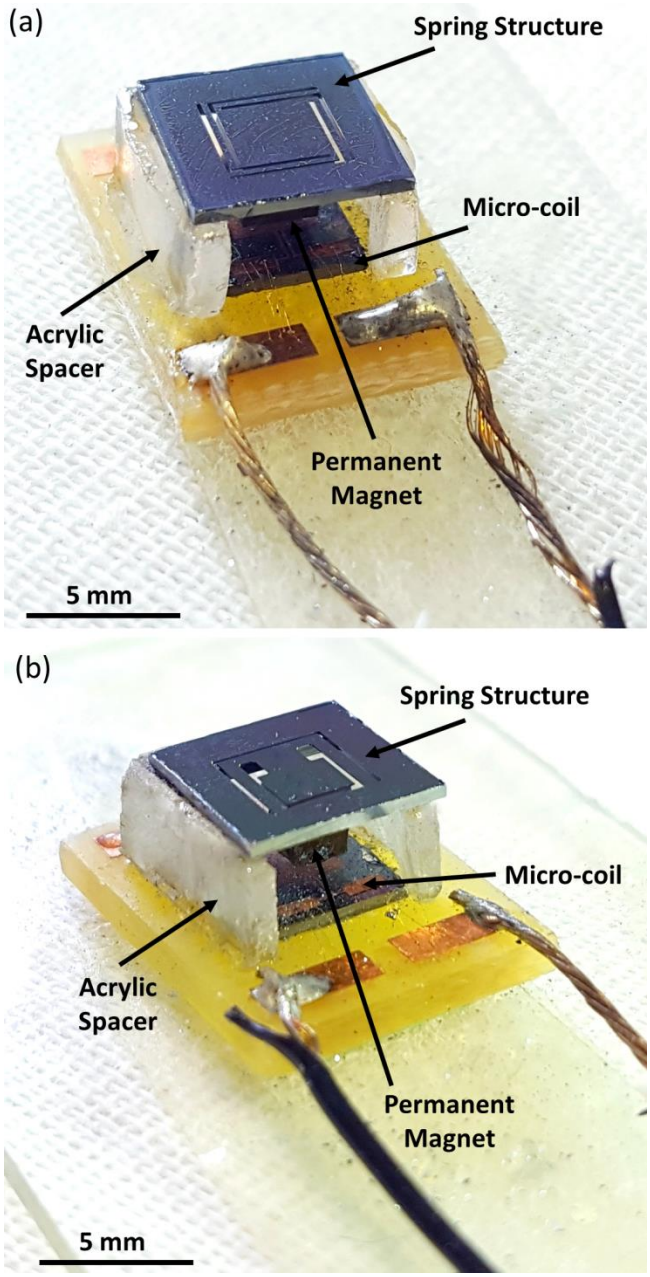

Fig. 10: Fabricated and fully packaged (a) single mass (SMD) MEMS harvester (b) dual mass (DMD) MEMS harvester

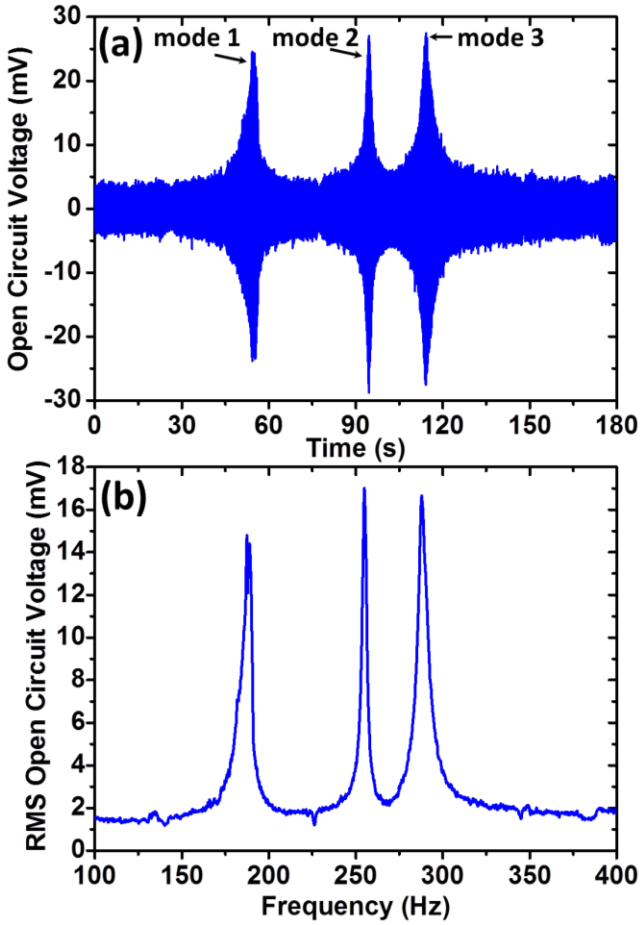

Fig. 11: (a) Time history for output open circuit voltage of the SMD as the input frequency is swept from 100 to 300 Hz at 0.5g. (b) The corresponding frequency response.

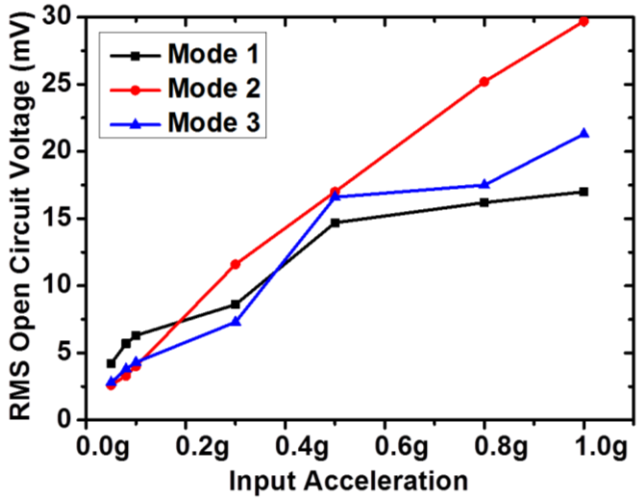

Fig 12: Variation of RMS open circuit voltage with the input acceleration.

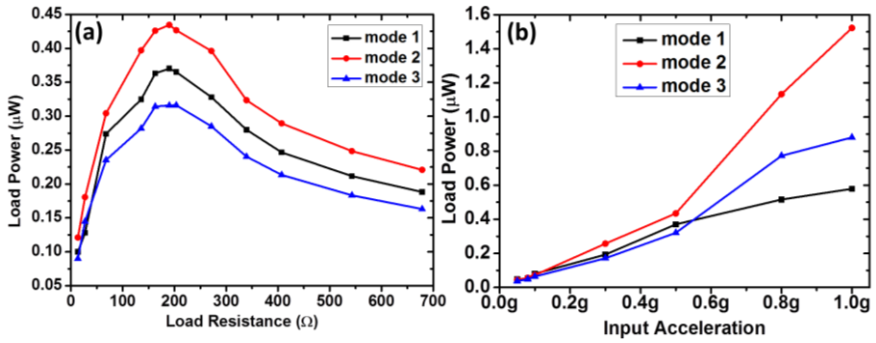

Fig. 13: (a) Variation of load power of the different modes of SMD with load resistance and (b) variation of load power with input acceleration.

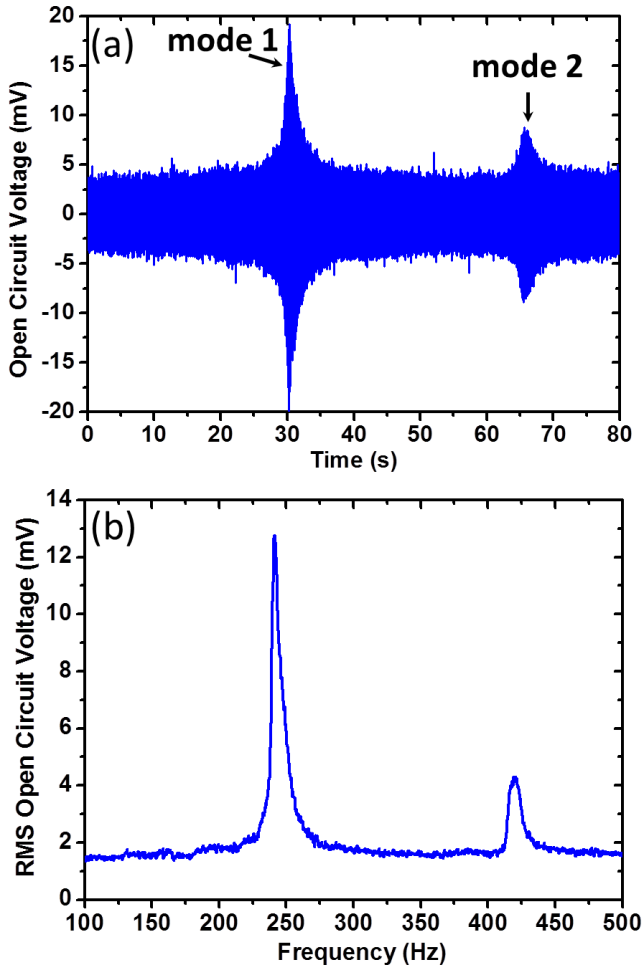

Fig. 14: (a) Time history for output open circuit voltage of the DMD as the input frequency is swept from 100 to 300 Hz at 0.5g. (b) The corresponding frequency response.

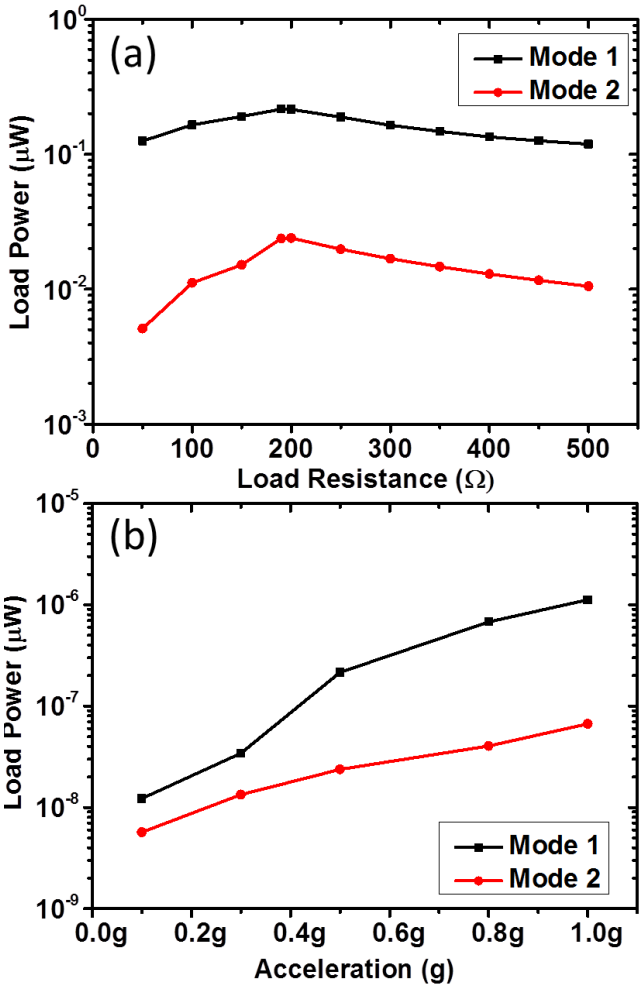

Fig. 15: (a) Variation of load power of the different modes of DMD with load resistance and (b) variation of load power with input acceleration.

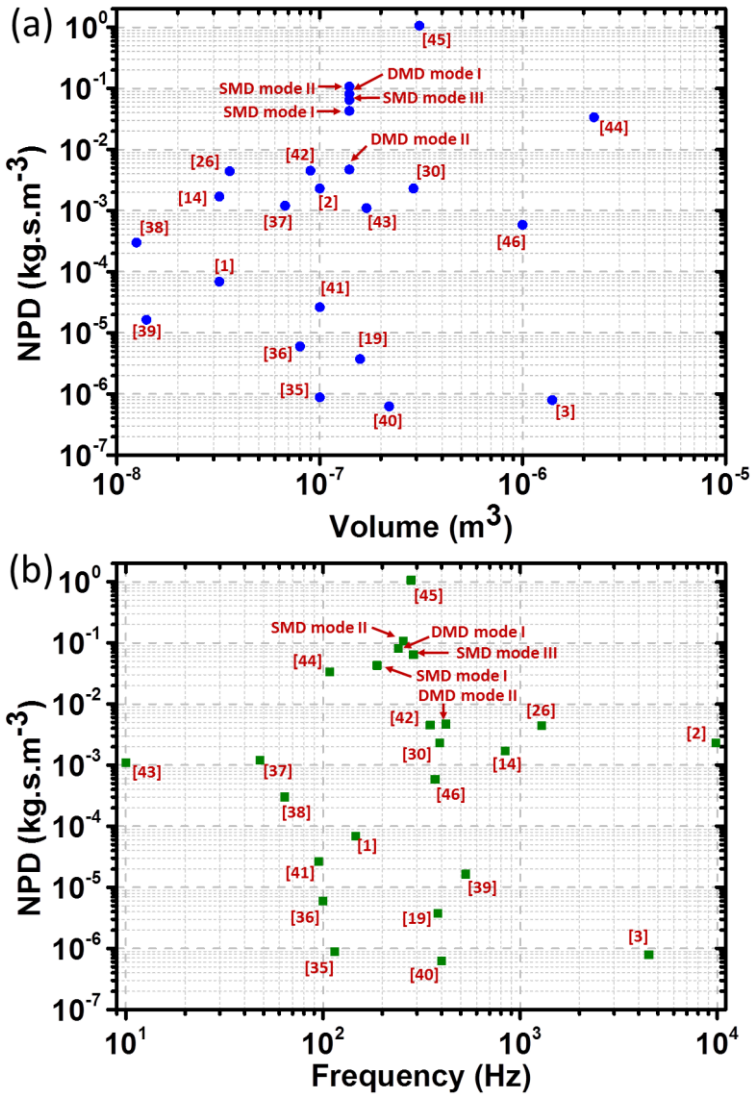

Fig. 16: Comparison of the Normalized Power Density (NPD) of the reported devices in different modes with the state-of-the-art MEMS EM VEH literatures in terms of (a) device volume and (b) operating frequency.

Table 1: Different parameters of the MEMS Single Mass Device (SMD)

Parameters	**Values**
Length of a single beam	3.45 mm
Width of the beams	0.2 mm
Thickness of the beams	50 μm
Dimension of movable paddle	$3\times3\times0.5$ mm^3
Mass attached (magnet)	9.83×10^{-5} kg
Magnet dimensions	$2.5\times2.5\times2$ mm^3
Coil footprint	2.8×2.8 mm^2
Coil no. of turns	144
Coil Resistance (R_C)	187 Ω
Gap between magnet and coil	0.8 mm

Table 2: Different parameters of the MEMS Dual Mass Device (DMD)

Parameters	**Values**
Length of the primary beam	3.25 mm
Width of the primary beam	1 mm
Length of the secondary beam	1 mm
Width of the secondary beam	1.5 mm
Thickness of the beams	50 μm
Primary Mass	2.5×10^{-6} kg
Secondary (magnet) Mass	68×10^{-6} kg
Magnet dimensions	$2\times2\times2$ mm^3
Coil footprint	2.8×2.8 mm^2
Coil no. of turns	144
Coil Resistance (R_C)	191 Ω
Gap between magnet and coil	0.8 mm

Table 3: Flux linkage constants for in-plane and out-of-plane motion of the magnet

Flux Linkage Constants	**In-plane motion**	**Out-of-plane motion**
a_3 (Wb/m^3)	4668.05	31574.84
a_2 (Wb/m^2)	74.23	-96.66
a_1 (Wb/m)	0.0143	0.17
a_0 (Wb)	-2.65×10^{-4}	-2.49×10^{-4}

Table 4: Comparison of experimental output performances of SMD and DMD

Output Parameters	**SMD**	**DMD**
Resonance Frequencies (Hz)	188 (mode I), 255.1 (mode II), 287.9 (mode III)	241.4 (mode I), 419.6 (mode II)
RMS Open Circuit Voltage at 0.5g (mV)	14.8 (mode I), 17.05 (mode II), 16.8 (mode III)	12.8 (mode I), 4.34 (mode II)
Matched Load (Ω)	190	190
Load Power at 0.5g (μW)	0.37 (mode I), 0.43 (mode II), 0.32 (mode III)	0.22 (mode I), 0.024 (mode II)
NPD (kg.s/m^3)	0.0429 (mode I), 0.1071 (mode II), 0.0643 (mode III)	0.0807 (mode I), 0.0047 (mode II)